Excellent Structural Stability Driven Cyclability in P2-type Ti-Based Cathode for Na-ion Batteries

Hari Narayanan Vasavan^a, Manish Badole^a, Samriddhi Saxena^a, Asish Kumar Das^a, Sonia

Deswal^b, Pradeep Kumar^b, and Sunil Kumar^{a,*}

^a Department of Metallurgy Engineering and Materials Science, Indian Institute of Technology
Indore, Simrol, 453552, India.

^b School of Physical Sciences, Indian Institute of Technology Mandi, Himachal Pradesh, 175005,

India

KEYWORDS: Layered Oxides; Na-ion batteries; Impedance; Electrochemical behavior; Cyclic performance

ABSTRACT. In the current study, we have synthesized Ti-based P2-type Na_{0.7}Ni_{0.2}Cu_{0.1}Ti_{0.65}O₂ (NNCT) through the sol-gel route and characterized it for its structural, electrical, and electrochemical properties. The analysis of X-ray diffraction (XRD) data confirmed the existence of a single P2 phase for the sample calcinated at 950 °C with suppressed Na-ion vacancy ordering. Impedance studies and chronoamperometric data revealed that NNCT exhibited a poor conductivity of $\sim 1.37 \times 10^{-7}$ S cm⁻¹ at room temperature, with the electronic conductivity

contribution to the total electrical conduction to be only 0.4%. The sample exhibited specific capacities of 83 mAh g⁻¹, 54 mAh g⁻¹, and 42 mAh g⁻¹ at discharge rates of 0.1C, 0.5C, and 1C, respectively, with a remarkable cyclic stability of 96% capacity retention after 700 cycles at 0.5C which makes NNCT an attractive cathode for Na-ion batteries in stationary storage applications. The ex-situ XRD analysis confirmed that NNCT maintains a single P2 phase during cycling between 2.0 V to 4.2 V. NNCT also exhibited moisture stability, thus enabling the use of a cost-effective water-based slurry for cathode layer fabrication.

1. INTRODUCTION

Na-ion batteries (NIBs) are often considered a viable alternative to Li-ion batteries (LIBs).¹⁻⁵ As demand for energy storage systems rises, due to the scarcity of Li deposits, Li-based battery systems are unlikely to be able to keep up with the demand, which would make them increasingly expensive.⁶⁻⁹ This makes the research into alternative energy storage systems essential for securing future energy needs. Na is a comparatively abundant natural resource, and batteries based on Na-ions share several communities with LIBs.^{6, 10, 11} This would make them easy to procure and eventually pay the way for their seamless integration of NIBs into the current battery manufacturing ecosystems.^{8, 12, 13}

Cathodes are the primary source of ions in a full-cell, and the kinetics of ions inside the cathode determines most of the properties, such as rate performance, cyclability, etc., of the cell.^{4, 14} In NIBs, prospective cathodes are broadly classified into 3 types NASICON, Layered Oxides, and Prussian Blue Analogues.^{13, 15} NASICON-type materials are known for their high cyclic stability but have a low specific capacity and are difficult to synthesize.^{3, 14} Prussian blue analogues compounds are novel cathodes with a cyanide group. These materials have been

reported to show specific capacities as high as 150 mAh g⁻¹ but are constrained by the inherent toxicity of cyanide ions. ^{16, 17} Layered oxides (LOs) are known for their compositional flexibility, seamless synthesis, and superior electrochemical performance compared to the other cathodes, ^{2, 14} which makes them the most popular option for replacing Li-ion-based cathodes in commercial Na-ion batteries. In addition, the current Li-ion battery technology also uses cathodes based on the layered oxide structure and shares many commonalities with Na-ion-based layered oxide cathodes. This would pave the way for their accelerated growth, as much of the data available on Li-ion-based cathodes can aid in advancing Na-based LOs, which is an added benefit.

LOs typically have a basic formula of Na_xTMO₂; $0 \le x \le 1$; TM- transition metal cation or a mixture of multiple cations, and are known to exist in a variety of phases like P2, P3 O3, O2, etc. This classification is based on the site configuration of Na-ions and the number of different O layers in the unit cell.¹⁸ O3-type LOs have $x \sim 1$ while P2 and P3 phases typically have x < 0.75.¹⁸⁻²⁰ With higher Na-ion concentrations, O3 phases usually show higher specific capacitates, while P2-type LOs fare better in rate and cyclic performance.²¹ This is due to the comparatively better open structure and resilience of P2-type LOs to phase transition, which improves Na-ion conduction dynamics in the material.²¹⁻²³

Over the past decade, researchers have been able to exploit the compositional flexibility of LOs by using different combinations of electrochemically active/inactive elements in the TM site to obtain better electrochemical properties.^{2, 4, 18} Among these, the combinations based on Na_xMnO₂ as the parent material have attracted tremendous attraction due to its higher specific capacity and greater availability.²⁴⁻²⁶ Recently, P2 type Na_xMnO₂ with a combination of Mn, Ni, and Cu in the TM site has shown considerably better cyclic stability with an initial specific capacity of 110 mAh g-1.²⁷⁻³² Even though Mn remains largely inactive during cycling, the

combination of Ni^{2+/4+} and Cu^{2+/3+} redox couples are able to make up for this shortfall. Moreover, as Ni and Cu ions maintain a 2+ oxidation state within the material, Mn is forced into a 4+ oxidation state, which is beneficial in eliminating the Jahn-teller active Mn³⁺. While Cu²⁺ is also Jahn-Teller active, Ni²⁺ is not; so, in Cu/Ni co-substituted (for Mn³⁺) materials, overall Jahn-Teller distortion decreases. The presence of Cu ions in the structure contributes towards better structural stability at higher voltages and moisture stability of the material.³³⁻³⁹ In addition, the presence of 3 different ions at the TM site also prevents the ordering of Na-ions vacancies and the transition metals, which can induce multiple phase transitions in LO cathode materials.⁴⁰⁻⁴²

Other substituents in the transition metal site include inactive dopants such as Zn, Ti, Mg, Al, Zr, etc. These are often referred to as pillar ions, as their sole function is to act as pillars of support upon the extraction of Na ions.^{33, 43-54} Since these ions do not participate in any charge compensation mechanisms during charging/discharging, the specific capacity of the material inevitably suffers, but other properties, such as rate performance and cyclability, have shown tremendous improvements with the inclusion of inactive substituents. This eventually can lead to these cathodes exhibiting better specific capacities than the parent material at relatively higher discharge rates, which can sometimes be as low as 0.1C. Several distortions to the crystal structure and particle morphology of the parent compound caused by introducing inactive substituents enable such property enhancements. For instance, in the case of Ti⁴⁺, we had reported that the presence of a larger ion (such as Ti-ions) in place of Mn4+ ions in Na_{0.7}Ni_{0.2}Cu_{0.15}Mn_{0.65}O₂ (NNCM)^{55, 56} led to the expansion of the unit cell and an increase in the area of the Na ion conduction bottlenecks. Consequently, the Na_{0.7}Ni_{0.2}Cu_{0.15}Mn_{0.575}Ti_{0.075}O₂ (NNCMT)⁵⁶ cathode also showed improvements in its particle morphology (such as the increased size of the lateral surface through a majority of the ionic conduction occurs) and

electrical properties which led to a remarkable improvement of 27% in the observed specific capacity of the parent compound at 0.1C rate which subsequently increased to about 50% at 1C.

Herein we report on the structural, electrical, and electrochemical properties of Na_{0.7}Ni_{0.2}Cu_{0.15}Ti_{0.65}O₂ (NNCT), which occupies the end member of the series where Ti⁴⁺ ions fully replace Mn⁴⁺ ions. The results obtained have been extensively compared with the parent material NNCM and NNCMT in hopes of establishing a trend of structural and electrochemical properties arising from Ti substitution.

2. EXPERIMENTAL SECTION

- 2.1. Synthesis. The synthesis of P2 type Na_{0.7}Ni_{0.2}Cu_{0.15}Ti_{0.65}O₂ was carried out using the solgel method. Stoichiometric amounts of manganese (II) acetate tetrahydrate, sodium carbonate (5% excess taken to compensate for losses during calcination), copper (II) nitrate trihydrate, nickel acetate tetrahydrate, and titanium (IV) bis(ammonium lactato)dihydroxide (50 wt.% aq.) were mixed in DI water. The solution was then stirred for 8 h, followed by adding ethylene glycol and citric acid. The resulting mixture was then allowed to stir for another 12 h, followed by heating to obtain a gel. The obtained gel was dried, ground to powder, and decarburized & denitrified at 550 °C in air. The resulting mixture was finally calcined at different temperatures (700 950 °C) for 12 h to obtain desired products.
- **2.2. Characterization.** X-ray diffraction technique (XRD) was used to study the crystal structure using a Malvern Pan analytical diffractometer (Empyrean) with a Cu-K $_{\alpha}$ source between a 2 θ range of 10°- 70° at room temperature. Rietveld refinement was used to analyze the crystal structure using the software package *TOPAS Academic* (version 6).⁵⁷ Morphology studies and elemental mapping of constituent elements in the powder samples were done using a field emission scanning electron microscopy (FESEM) (model JEOL-7610) equipped with

energy-dispersive x-ray spectroscopy (EDS). A Thermofisher Scientific-Naxsa (Al-Kα source) was used for X-ray photoelectron spectroscopy (XPS) measurements.

Impedance studies were conducted on a pelletized sample sintered at 950 °C. A LCR meter (model: ZM 2376, NF Corp.) was employed to obtain the complex impedance data by applying a 50 mV ac signal in a frequency range of 1 Hz – 1 MHz. The chronoamperometry was performed with the help of a Source Meter Unit (model: Keithley 2450-EC) to estimate the transference number by applying a voltage of 1 V.

The cathodes for electrochemical experiments were fabricated by coating a slurry consisting of the active material, Ketjen black, and CMC binder in DI water in the wt. ratio of 80:10:10 on an aluminum current collector, which was then dried and punched into 16 mm disks. These cathodes were assembled in a CR-2032 coin cell in a half-cell configuration with 1M NaBF₄ in tetraethylene glycol dimethyl ether (tetraglyme) as the electrolyte and a Celgard 2400 membrane as the separator. Cyclic voltammetry (CV) was performed using the Source Meter Unit (model: Keithley 2450-EC) between 2.00 V to 4.20 V at a scan rate of 0.1 mV s⁻¹, and a Landt LANHE CT, 2001A tester was employed for conducting galvanometric charge-discharge (GCD) tests. All C-rates were calculated by assuming a specific capacity of 120 mAh g⁻¹, and the active mass loading of the cathode was around 2 mg cm⁻².

3. RESULTS AND DISCUSSION

3.1. XRD. Figure 1(a) displays the XRD patterns of NNCT at different calcination temperatures between 700 °C – 950 °C. The figure shows the emergence of O3 and P3 type phases (along with impurity peaks related to other unreacted phases) at 850 °C and 900 °C which is concurrent with the findings in NNCMT samples where a minor O3 phase (JCPDS:09- 0063) was detected upon Ti substitution. The total phase fraction of both these phases was estimated to be less than 10%

of the total sample. Upon increasing the calcination temperature to about 950 °C, O3 and P3 phases disappeared, and a single P2 phase (JCPDS:27- 0751) was obtained. This was confirmed by Rietveld refinement of the room temperature XRD data of the sample calcinated at 950 °C, which shows the existence of a single P2 phase in a P63/mmc space group (Figure 1(b)). The hexagonal unit cell was found to have a volume of 85.142 ± 0.004 ų with lattice parameters $a = 2.96573 \pm 0.00005$ Å, $c = 11.1772 \pm 0.0002$ Å. The crystallographic parameters used in Rietveld refinement are displayed in Table 1. The disappearance of the O3 and P3 phases with temperature could be related to the volatilization of Na and the conversion of the P3-type structure to a P2-type structure at higher synthesis temperatures. For the sample synthesized at 950 °C, a minor impurity phase (a small peak at $20 \sim 36^\circ$ in Fig. 1(a), possibly a CuO phase) was observed along with the dominant P2 phase. As the fraction of this impurity phase was < 1 wt.%, it was ignored in further discussion.

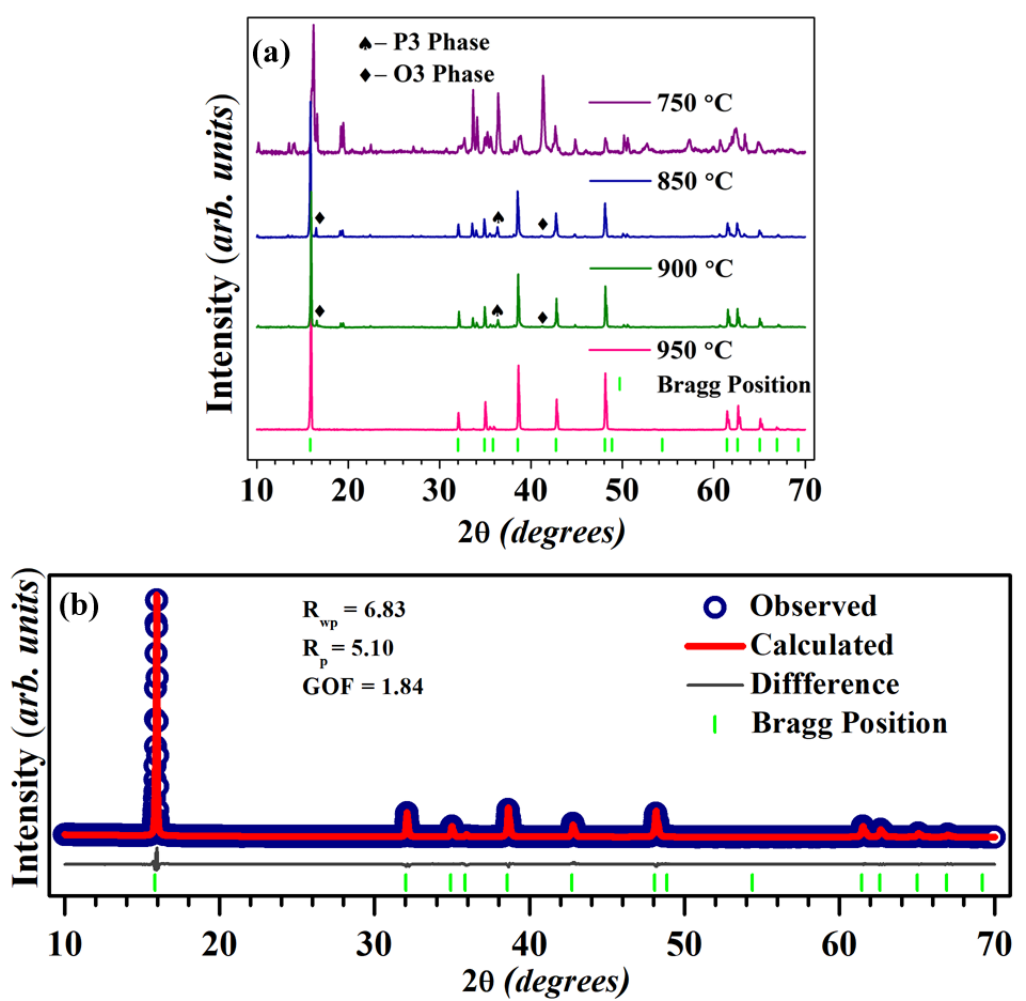


Figure 1. (a) XRD patterns illustrating the phase evolution of NNCT with calcination temperature recorded at room temperature. (b) Rietveld refinement profile of room temperature XRD data, for the NNCT powder sample calcinated at 950 °C.

Table. 1. Crystallographic parameters of P2-NNCT sample calcinated at 950 °C.

Atom	X	y	Z	Occupancy	Site
Na1	2/3	1/3	1/4	0.45	2d
Na2	0	0	1/4	0.25	2b
Ti/ Ni/ Cu	0	0	0	0.65/0.20/0.15	2a
0	2/3	1/3	0.09	1	4f

Compared to NNCT, NNCM and NNCMT LOs showed lower cell volumes and unit cell parameters. 55, 56 This is expected as Ti4+ ions (0.605 Å in 6 coordination) have a higher ionic radius compared to the Mn⁴⁺ ions (0.530 Å in 6 coordination), which would expand the unit cell, increasing its volume and is reported in the literature. 58-60 The Vesta software package 61 was used to generate the 3D image visualization of the NNCT unit cell using the refined parameters and is displayed in Figure 2. The volume of the TM-O6 octahedron and Na-O6 prism in the layered oxide structure were calculated to be around 10.44 Å³ and 13.45 Å³, respectively. In NNMC and NNMCT, however, the TM-O₆ octahedra showed a lower volume (8.53 $Å^3$ and \sim 8.45 Å³, respectively), while Na-O₆ prism had a higher volume (13.83 Å³ and 14.09 Å³, respectively). Consequently, the area of the rectangular face of Na–O₆ (10.47 Å²) in NNCT was about 10-11% lower than the other samples. This face forms one of the primary bottlenecks for the Na-ion conduction through LOs. The lower area of this plane in NNCT indicates the possibility of lower Na-ion conduction that could limit its rate performance. Also, contrary to NNCM, the absence of superlattice peaks in NNCT at ~ 27.2° and 28.3° in the XRD patterns caused by Na-ion vacancy ordering shows a highly disordered Na-ion structure. Na-ion vacancy ordering is a known phenomenon that induces various structural transformations of the cathode during cycling, severely limiting its cyclability. 40-42 The absence of Na-ion vacancy ordering in NNCT could enhance the structural stability of the NNCT unit cell during cycling, leading to better cyclic stability and Na-ion conduction through the material.

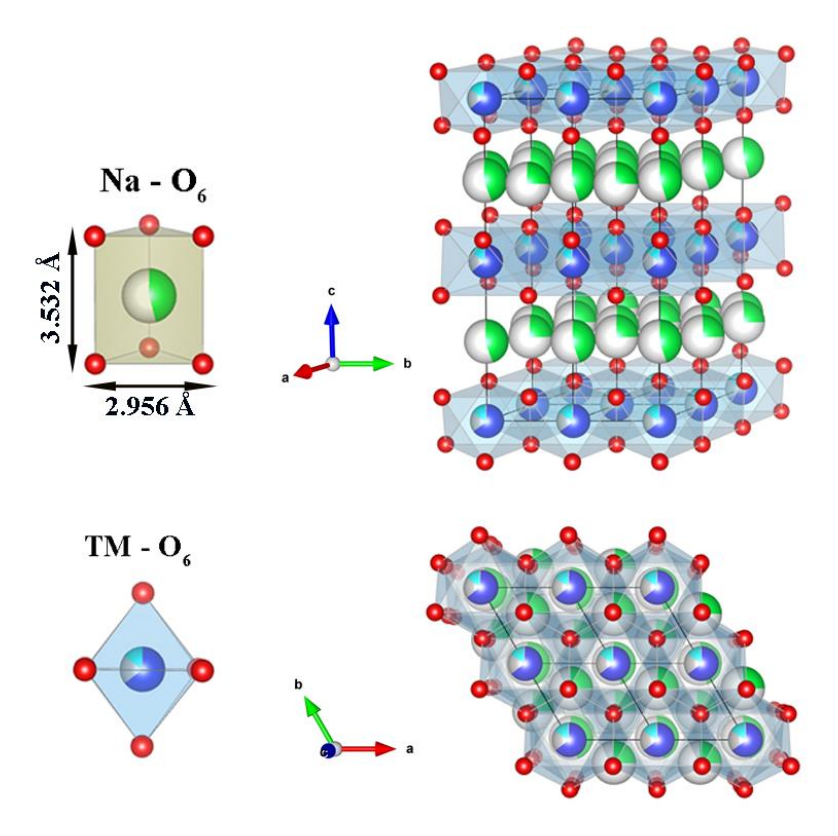


Figure 2. Crystal structure visualization of P2-type NNCT.

3.2. Scanning Electron Microscopy (SEM). Figure 3(a) shows the cross-sectional SEM image of the NNCT fractured pellet. The SEM micrograph of the powered sample (calcinated at 950 °C) is presented in Figure 3(b). The image of the powder sample shows particles with irregularly shaped polyhedra, possibly formed due to the agglomeration of individual particles. This is in sharp contrast to the hexagonal plates observed in NNMC and NNMCT samples, where an increase in the area of the $(\bar{1}00)$ $(0\bar{1}0)$, $(0\bar{1}0)$ $(\bar{1}00)$ was observed with an increase in Ti concentration which was instrumental in improving the rate performance of the parent NNMC cathode sample. However, the elemental maps of the sample (Figure 3(b1-b5)) do not show any segregation of the constituent elements in the material. The SEM micrograph showing the cross-sectional of the sintered pellet indicates tightly packed and randomly oriented particles. The relative density of the pellet was estimated to be around 90 ± 2 %.

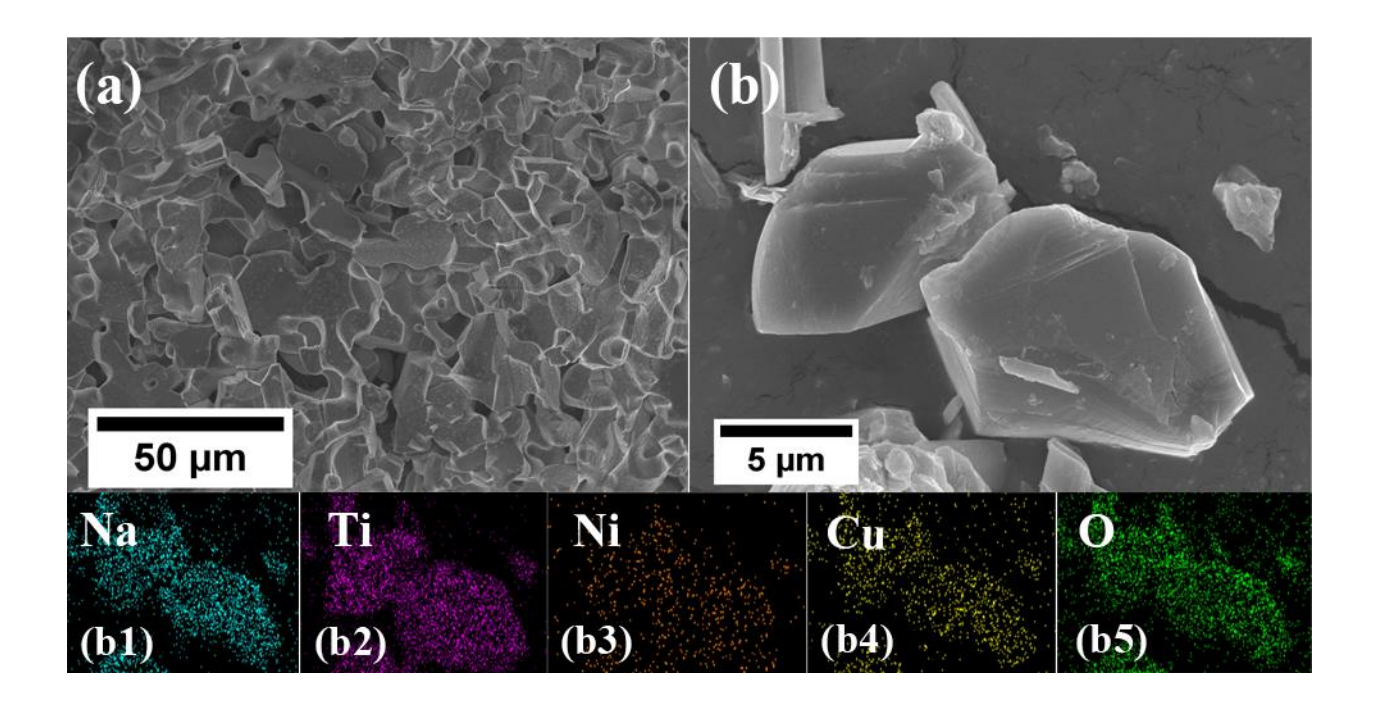


Figure 3. SEM micrographs of the NNCT (a) fractured pellet sintered at 950 °C (b) powder sample. (b1) - (b5) elemental maps of NNCT showing the distribution of its constituent elements.

3.3. X-ray photoelectron spectroscopy (XPS). XPS data used to ascertain the oxidation states of the transition metal elements in the sample obtained spectra of Cu 2p, Ni 2p, and Ti 2p are depicted in Figure 4. The Ni2p spectrum shows four peaks which belong to Ni 2p_{3/2} (~ 855 eV) and Ni 2p_{1/2}(~ 872 eV) and their respective satellites, confirming the presence of Ni²⁺.^{28, 62, 63} The Cu 2p spectrum shows 2 peaks at 933 eV (characteristic of Cu 2p_{3/2}) and at 953 eV (attributed to Cu 2p_{1/2}), indicating Cu²⁺ in the materials.^{28, 62, 63} The characteristic peaks at 458 and 464 eV in the Ti 2p spectrum are attributed to Ti 2p_{3/2} and Ti 2p_{1/2} which suggest that Ti maintains a 4+ oxidation state in the material.^{62, 63}

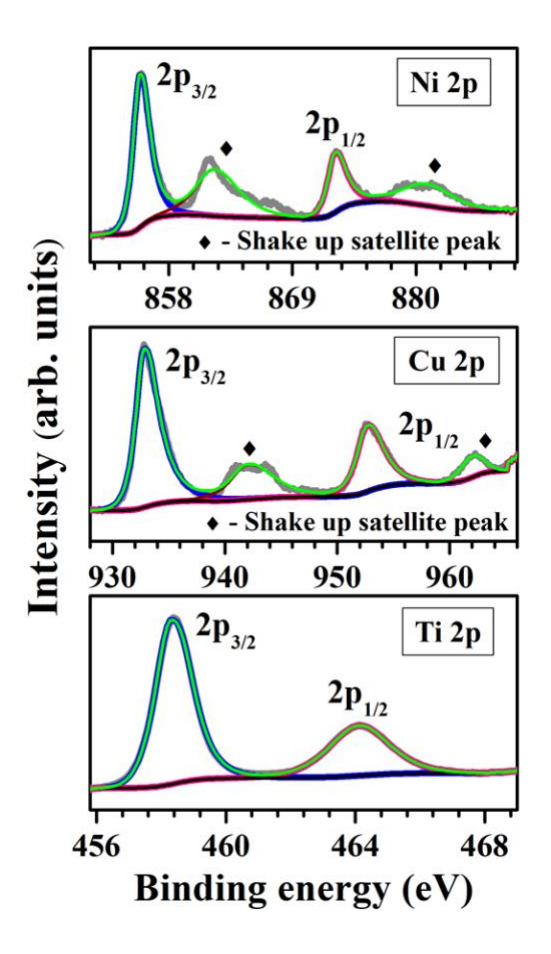


Figure 4. XPS spectra of as-prepared Na_{0.7}Ni_{0.20}Cu_{0.15}Ti_{0.65}O₂ sample.

3.4. Electrical Properties. To investigate the transport phenomenon through the material, Complex Impedance Spectroscopy was performed on the pelletized sample sintered at 950 °C for 12 h. Figure 5(a) shows the Nyquist plots depicting the impedance data at different temperatures. A temperature-independent tail component observed at low frequencies in the Nyquist plot suggests ion-blocking by the silver electrodes and is indicative of substantial ionic conduction through the material. A decreasing trend of the overall resistance of the sample with an increase in temperature is also evident in the figure. Equivalent circuit modelling (Figure 5(a) insert) was used to analyze the Nyquist plot and estimate the conductivity of the sample. The room temperature conductivity of the NNCT sample was estimated to be about 1.37×10^{-7} S cm⁻¹. In

comparison, NNCM showed a room temperature conductivity of $\sim 4.03 \times 10^{-6} \text{ S cm}^{-1}$ and it increased to $3.07 \times 10^{-5} \text{ S cm}^{-1}$ in the Ti substituted NNCMT sample, both of which are considerably higher than that of the NNCT. Linear fitting of temperature-dependent conductivity values using the Arrhenius equation (equation 1) was used to estimate the activation energy (E_A) of the overall sample (Figure 5 (b)).

$$\sigma(T) = \sigma_o \ e^{-(\frac{E_A}{kT})} \tag{1}$$

Here σ_0 is the pre-exponential factor, k is Boltzmann's constant, and T is the absolute temperature. The activation energy of the sample was calculated to be about 0.41 ± 0.02 eV which is about twice the value reported for the manganese analog Na_{0.7}Ni_{0.2}Cu_{0.1}Mn_{0.65}O₂ sample.⁵⁵ This suggests poor ion conduction dynamics of the NNCT cathode, resulting from the lower area of the conduction bottlenecks and the irregular particle morphology observed earlier. The diffusion coefficient of the NNCT sample calculated using the Nernst Einstein relation at 310 K (equation 2) was around 1.94×10^{-16} m² s⁻¹.

$$D = \frac{kT}{Nq^2} \sigma_{DC} \tag{2}$$

N is the number density of charge carriers per unit volume of the unit cell, and q is the elementary charge. Even though the diffusion coefficient for NNCT is lower than that of NNCM and NNCMT cathodes, it is comparable to other cathodes such as Na_{0.67}Mn_{0.65}Ni_{0.2}Co_{0.15}O₂, Na_{0.67}Mn_{0.55}Ni_{0.25}Li_{0.2}O₂, Na_{2/3}Ni_{1/3}Mn_{5/9}Al_{1/9}O₂, etc. reported in literature.⁶⁴⁻⁶⁶ However, the chronoamperometric data (Figure 5(c)) of the NNCT put the electron transference number (t_e) of the sample at 0.004 and Na⁺ transference number (t_{Na}) at 0.996, which suggests significantly low electronic conduction through the material. This is typically observed in materials containing d⁰ ions, such as Ti⁴⁺, as the ion is relatively stable in the current configuration and does not donate

its electrons to the conduction band, drastically bringing down the electronic conduction. The poor electronic conduction coupled with lower ionic conductivity would adversely affect the rate performance of the NNCT cathode during cycling.

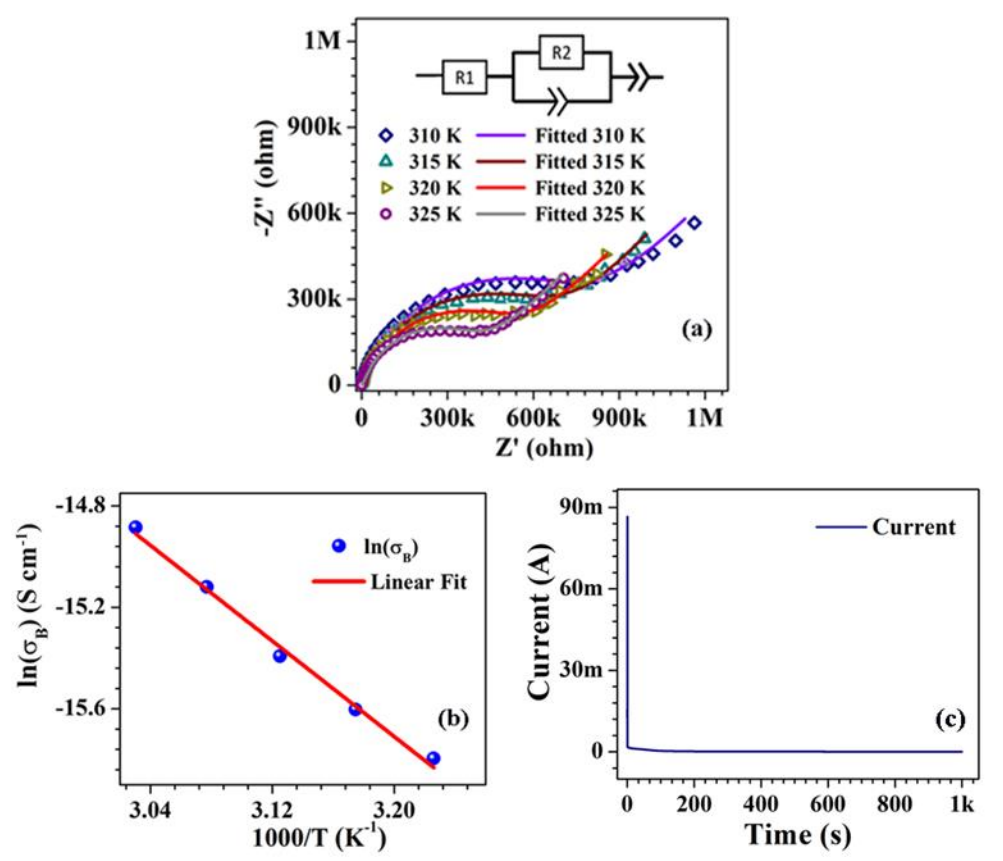


Figure 5. Electrical properties of NNCT. (a) Nyquist plots at different temperatures and their fitted curves, modeled using the equivalent circuit shown as an inset. (b) Arrhenius plot showing temperature dependence of electrical conductivity. (c) Chronoamperometry curve of NNCT under an applied potential of 1 V.

3.5. Electrochemical Properties. Figure 6(a) depicts the cyclic voltammetric curves of the NNCT cathode between 2 V to 4.2 V at a scan rate of 0.1 mV s⁻¹. The curve portrays a broad peak at 3.7 V, which can be attributed to the Ni^{2+/4+} and Cu^{2+/3+} redox couples.^{58, 67} On the other hand, the NNCT and NNCMT samples showed 2 distinct peaks for Ni^{2+/4+} and Cu^{2+/3+} reactions

between 3.3 V and 4.0 V, along with some vacancy ordering peaks, particularly in NNCM. This could be due to a comparatively higher disordering in the NNCT structure that inhibits Navacancy ordering. Ti maintains a 4+ oxidation state within the voltage range and acts like pillar ions supporting the structure during the extraction/ intercalation of Na-ions. The dQ/dV vs. voltage graphs are presented in figure 6(b) and show that the peak (at ~ 3.6 V at 1C rate) shifts toward higher voltages with an increase in the C-rate.

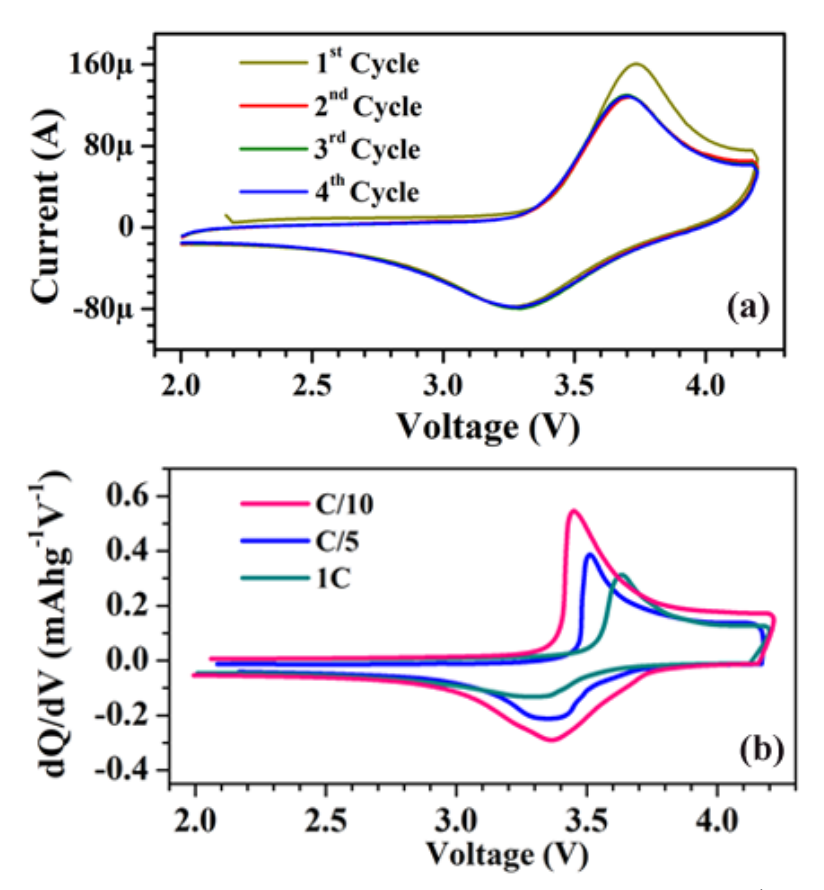


Figure 6. Cyclic voltammogram of NNCT at a scan rate of 0.1 mV s⁻¹.

Figure 7(a) shows the galvanostatic charge/discharge curves of NNCT at different C rates between 2 V to 4.2 V. The curve depicts a higher slope between 2 - 3 V compared to 3 - 4.2 V. This is due to the unavailability of the redox process in the lower voltage regions compared to the higher voltage ranges where $Ni^{2+/4+}$ and $Cu^{2+/3+}$ redox processes become active. At a

comparatively lower discharge rate of 0.1C, the NNCT cathode shows a specific capacity of 83 mAh g⁻¹, which drops to 54 mAh g⁻¹ and 42 mAh g⁻¹ at 0.5C and 1C, respectively. The rate performance of the cathode at different discharge rates between 0.1C and 2C is displayed in Figure 7(b). In contrast, the NNMC cathode showed a specific capacity of 99 mAhg⁻¹ and 64 mAh g⁻¹ at 0.1C and 1C discharge rates, which was increased to 127 mAh g⁻¹ and 96 mAh g⁻¹ upon Ti substitution in the NNMCT sample. Even at a discharge rate of 2C, a specific capacity of 87 mAh g⁻¹ could be obtained from the latter. The comparatively high reduction in specific capacity with an increase in discharge rate in the NNCT cathode sample can be attributed to the unfavorable structural properties, lower electrical conductivity, and t_e values discussed in the electrical properties section. In terms of cyclability, however, the cathode shows much better performance, with 96% of the initial capacity retained after 700 cycles at a charge/discharge rate of 0.5C with a median discharge voltage \sim 3.2 V. (Figure 7(c)). This points to a remarkable resilience of the NNTC unit cell to distortions induced by repeated extraction/intercalation of Na ions during each cycle.

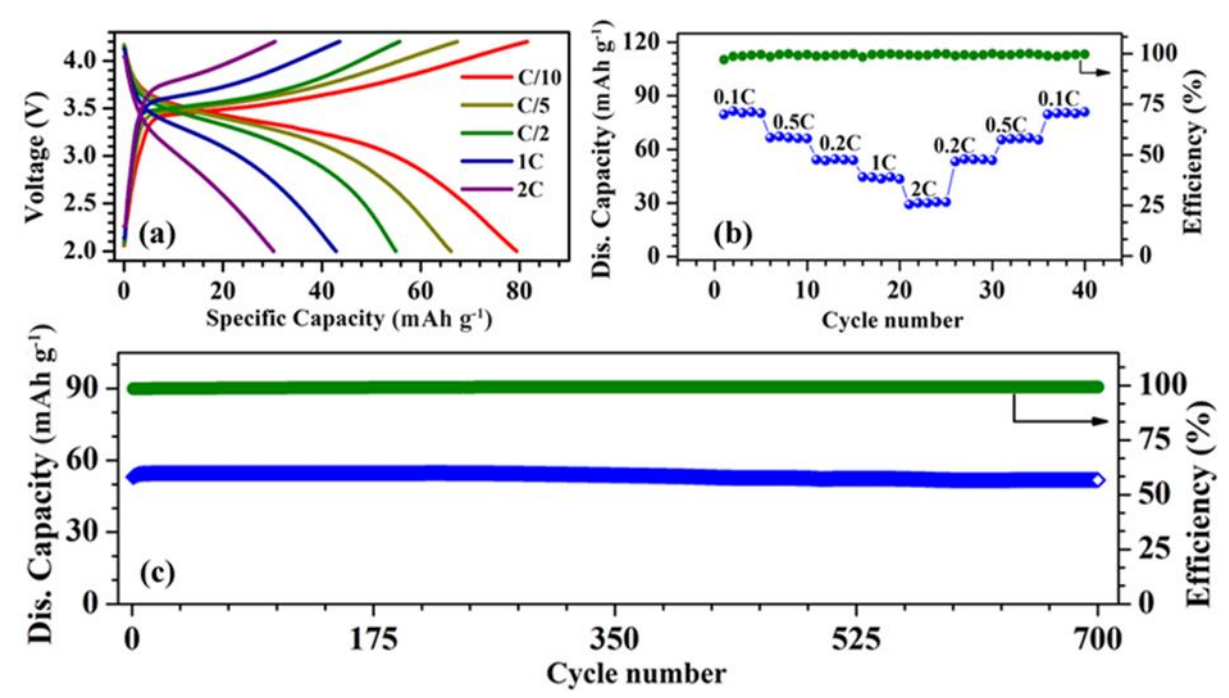


Figure 7. (a) Galvanometric charge-discharge curves. (b) Rate performance of NNCT cathode at different discharge rates. (c) Cyclic performance of NNCT at 0.5C for 700 cycles.

To investigate the changes in structural parameters during cycling, ex-situ XRD was performed on the cathodes at different states-of-charge (Figure 8(a)). The data show an expansion of the unit cell with charging as illustrated by the shifting of the (002) and (004) peaks towards lower diffraction angles (Figure 8(a1, a2)).^{27, 45, 68} This trend was also observed in the NNCM and NNCMT cathodes due to the increased repulsion between oxygen layers in the LO structure after Na ions are extracted. These peaks return to their original positions upon discharging, implying the reversibility of the structural changes occurring during GCD cycling. The moisture sensitivity of the sample was tested by storing the cathode powder in DI water for 1 week. The XRD patterns of the dried water-treated samples showed no changes compared to that of the untreated sample (Figure 8(b)). This has allowed the use of CMC as the binder and DI water as the solvent. In addition, the excellent moisture stability of the cathode also meant that the as-

synthesized sample could be stored in ambient conditions. Both these factors would considerably reduce the fabrication cost of cells.

Although the NNCT cathode shows excellent cycle stability, a property highly sought after in cathodes, its specific capacity at 0.1C is only about 56% of its theoretical capacity (146 mAh g⁻¹). This could be due to its unfavorable structural and electrical properties discussed above, and this material could show considerably higher specific capacities at lower discharge rates (0.05C and lower). However, keeping the real-world applications in mind, the specific capacity of NNCT should be further improved at relevant C-rates (0.2C to 2C). As lower electronic and ionic conductivities seem to be the limiting factor for observed specific capacities, techniques such as in-situ carbon coating, tailoring the particle morphology of NNCT particles, etc., could be explored to address these issues. Nevertheless, excellent cycle stability makes NNCT an attractive candidate for Na-ion batteries in stationary storage applications.

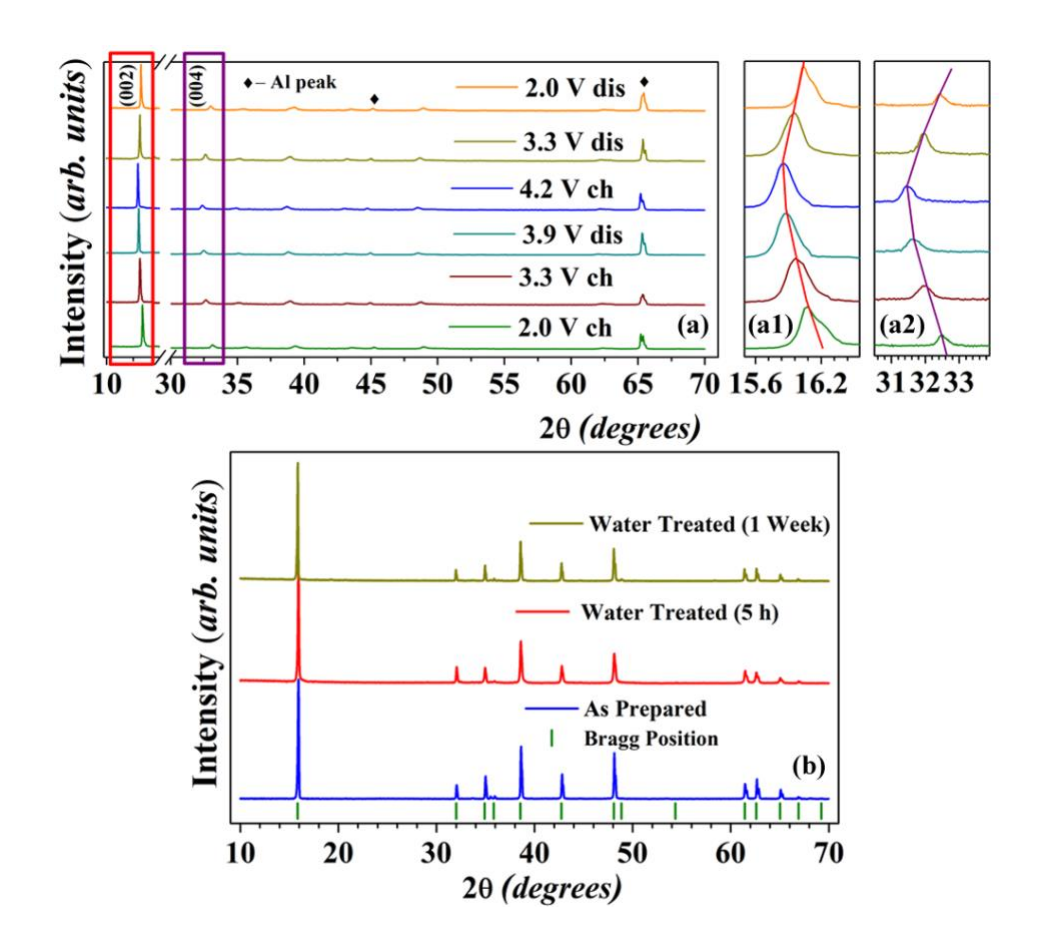


Figure 8. (a) Ex-situ XRD patterns of NNCT cathode during charge(ch)/discharge(dis) cycle at 0.1C between 2.0 V to 4.2 V. (a1) and (a2) show the enlarged portion of the patterns in the vicinity of (002) and (004) peaks. The peaks marked by ♦ belong to the Al current collector. (b) XRD patterns of as-prepared NNCT powder before and after being treated with water.

4. CONCLUSIONS

In summary, P2-type Na_{0.7}Ni_{0.2}Cu_{0.15}Ti_{0.65}O₂, which is at the extreme end of the Na_{0.7}Ni_{0.2}Cu_{0.15}Mn_{0.65-x}Ti_xO₂ series, was synthesized through the sol-gel route. Rietveld refinement of XRD data confirmed a single P2 phase for the NNCT sample calcinated at 950 °C having smaller Na-ion conduction bottlenecks compared to Na_{0.7}Ni_{0.2}Cu_{0.15}Mn_{0.65}O₂ and Na_{0.7}Ni_{0.2}Cu_{0.15}Mn_{0.575}Ti_{0.075}O₂ samples, while the SEM micrographs exhibited irregularly

shaped NNCT particles with a uniform elemental distribution. Impedance studies on the pelletized sample were used to investigate the electrical properties of the material. The electrical conductivity of the sample was estimated to be around 1.37×10^{-7} S cm⁻¹, while the activation energy was found to be ~ 0.41 eV. The sample also showed poor electronic conduction with chronoamperometric data putting the electronic transference number (t_e) at 0.004. During electrochemical testing, the NNCT sample delivered a capacity of 83 mAh g⁻¹ at a discharge rate of 0.1C, decreasing to 54 mAh g⁻¹ and 42 mAh g⁻¹ at 0.5C and 1C, respectively. The increased capacity degradation is attributed to the low electrical conductivity and t_e values of the NNCT sample. The sample, however, exhibited excellent cyclic stability with 96% initial capacity retained after 700 cycles at 0.5C. The cathode maintained a single P2 phase between 2.00 V to 4.20 V during cycling and was also found to be moisture stable.

AUTHOR INFORMATION

Corresponding Author

Sunil Kumar - Department of Metallurgy Engineering and Materials Science, Indian Institute of Technology Indore, Simrol, 453552, India; E-mail address: sunil@iiti.ac.in; Tel: +91-7324306-685

Authors

Hari Narayanan Vasavan - Department of Metallurgy Engineering and Materials Science, Indian Institute of Technology Indore, Simrol, 453552, India.

Manish Badole - Department of Metallurgy Engineering and Materials Science, Indian Institute of Technology Indore, Simrol, 453552, India.

Samdriddhi Saxena - Department of Metallurgy Engineering and Materials Science, Indian Institute of Technology Indore, Simrol, 453552, India.

Asish Kumar Das - Department of Metallurgy Engineering and Materials Science, Indian Institute of Technology Indore, Simrol, 453552, India.

Sonia Deswal - School of Physical Sciences, Indian Institute of Technology Mandi, Himachal Pradesh, 175005, India.

Pradeep Kumar - School of Physical Sciences, Indian Institute of Technology Mandi, Himachal Pradesh, 175005, India.

Notes

The authors declare no conflict of interests.

ACKNOWLEDGMENTS

The authors thank Science and Engineering Research Board (SERB), India, for the financial support (grant number: CRG/2021/005548).

REFERENCES

(1) Buchholz, D.; Moretti, A.; Schmuch, R.; Nowak, S.; V, S.; M, W.; Passerini, S. Towards Na-ion batteries – Synthesis and Characterization of a novel high capacity Na-ion intercalation material. *Chem. Inform* **2013**, *160*, 44. https://doi.org/10.1002/chin.201319014.

- (2) Darga, J.; Lamb, J.; Manthiram, A. Industrialization of Layered Oxide Cathodes for Lithium-Ion and Sodium-Ion Batteries: A Comparative Perspective. *Energy Technol.* **2020**, *8* (12), 2000723. https://doi.org/10.1002/ente.202000723.
- (3) Usiskin, R.; Lu, Y.; Popovic, J.; Law, M.; Balaya, P.; Hu, Y.-S.; Maier, J. Fundamentals, status and promise of sodium-based batteries. *Nature Rev. Mater.* **2021**, *6* (11), 1020-1035. https://doi.org/10.1038/s41578-021-00324-w.
- (4) Clément, R. J.; Bruce, P. G.; Grey, C. P. Review—Manganese-Based P2-Type Transition Metal Oxides as Sodium-Ion Battery Cathode Materials. *J. Electrochem. Soc.* **2015**, *162* (14), A2589-A2604. https://doi.org/10.1149/2.0201514jes.
- (5) Zhu, Y.-F.; Xiao, Y.; Dou, S.-X.; Kang, Y.-M.; Chou, S.-L. Spinel/Post-spinel engineering on layered oxide cathodes for sodium-ion batteries. *eScience* **2021**, *I* (1), 13-27. DOI: https://doi.org/10.1016/j.esci.2021.10.003.
- (6) *Mineral commodity summaries 2021*; Reston, VA, 2021. http://pubs.er.usgs.gov/publication/mcs2021 https://doi.org/10.3133/mcs2021.
- (7) Larcher, D.; Tarascon, J. M. Towards greener and more sustainable batteries for electrical energy storage. *Nature Chem.* **2015**, *7* (1), 19-29. https://doi.org/10.1038/nchem.2085.
- (8) Hwang, J.-Y.; Myung, S.-T.; Sun, Y.-K. Sodium-ion batteries: present and future. *Chem. Soc. Rev.* **2017**, *46* (12), 3529-3614. DOI: https://doi.org/10.1039/C6CS00776G.
- (9) Wang, C.; Tan, L.; Yi, H.; Zhao, Z.; Yi, X.; Zhou, Y.; Zheng, J.; Wang, J.; Li, L. Unveiling the impact of residual Li conversion and cation ordering on electrochemical performance of Co-free Ni-rich cathodes. *Nano Research* **2022**, *15* (10), 9038-9046 https://doi.org/10.1007/s12274-022-4889-0.
- (10) Vaalma, C.; Buchholz, D.; Weil, M.; Passerini, S. A cost and resource analysis of sodium-ion batteries. *Nature Rev. Mater.* **2018**, *3* (4), 18013. DOI: https://doi.org/10.1038/natrevmats.2018.13.
- (11) Peters, J.; Cruz, A.; Weil, M. Exploring the Economic Potential of Sodium-Ion Batteries. *Batteries* **2019**, *5*, 10. https://doi.org/10.3390/batteries5010010.

- (12) Palomares, V.; Serras, P.; Villaluenga, I.; Hueso, K. B.; Carretero-González, J.; Rojo, T. Na-ion batteries, recent advances and present challenges to become low cost energy storage systems. *Energy Environ. Sci.* **2012**, *5* (3), 5884-5901, 10.1039/C2EE02781J. https://doi.org/10.1039/C2EE02781J.
- (13) Xiang, X.; Zhang, K.; Chen, J. Recent Advances and Prospects of Cathode Materials for Sodium-Ion Batteries. *Adv. Mater.* **2015**, *27* (36), 5343-5364. https://doi.org/10.1002/adma.201501527.
- (14) Goikolea, E.; Palomares, V.; Wang, S.; de Larramendi, I. R.; Guo, X.; Wang, G.; Rojo, T. Na-Ion Batteries—Approaching Old and New Challenges. *Adv. Energy Mater.* **2020**, *10* (44), 2002055. https://doi.org/10.1002/aenm.202002055.
- (15) Kundu, D.; Talaie, E.; Duffort, V.; Nazar, L. F. The Emerging Chemistry of Sodium Ion Batteries for Electrochemical Energy Storage. *Angew. Chem. Int. Ed.* **2015**, *54* (11), 3431-3448. https://doi.org/10.1002/anie.201410376.
- (16) Kjeldgaard, S.; Dugulan, I.; Mamakhel, A.; Wagemaker, M.; Iversen, B. B.; Bentien, A. Strategies for synthesis of Prussian blue analogues. *R. Soc. Open Sci.* **2021**, *8* (1), 201779. https://doi.org/10.1098/rsos.201779.
- (17) Du, G.; Pang, H. Recent advancements in Prussian blue analogues: Preparation and application in batteries. *Energy Storage Mater.* **2021**, *36*, 387-408. https://doi.org/10.1016/j.ensm.2021.01.006.
- (18) Delmas, C.; Fouassier, C.; Hagenmuller, P. Structural classification and properties of the layered oxides. *Physica B+C* **1980**, *99* (1), 81-85. https://doi.org/10.1016/0378-4363(80)90214-4.
- (19) Zhao, C.; Yao, Z.; Wang, Q.; Li, H.; Wang, J.; Liu, M.; Ganapathy, S.; Lu, Y.; Cabana, J.; Li, B.; et al. Revealing High Na-Content P2-Type Layered Oxides as Advanced Sodium-Ion Cathodes. *J. Am. Chem. Soc.* **2020**, *142* (12), 5742-5750. https://doi.org/10.1021/jacs.9b13572.
- (20) Wang, P.-F.; You, Y.; Yin, Y.-X.; Wang, Y.-S.; Wan, L.-J.; Gu, L.; Guo, Y.-G. Suppressing the P2–O2 Phase Transition of Na_{0.67}Mn_{0.67}Ni_{0.33}O₂ by Magnesium Substitution for Improved Sodium-Ion Batteries. *Angew. Chem. Int. Ed.* **2016**, *55* (26), 7445-7449. https://doi.org/10.1002/anie.201602202.

- (21) Liu, J.; Kan, W. H.; Ling, C. D. Insights into the high voltage layered oxide cathode materials in sodium-ion batteries: Structural evolution and anion redox. *J. Power Sources* **2021**, *481*, 229139. https://doi.org/10.1016/j.jpowsour.2020.229139.
- (22) Liu, Z.; Xu, X.; Ji, S.; Zeng, L.; Zhang, D.; Liu, J. Recent Progress of P2-Type Layered Transition-Metal Oxide Cathodes for Sodium-Ion Batteries. *Chem. Eur. J.* **2020**, *26* (35), 7747-7766. https://doi.org/10.1002/chem.201905131.
- (23) Guo, S.; Sun, Y.; Yi, J.; Zhu, K.; Liu, P.; Zhu, Y.; Zhu, G.-z.; Chen, M.; Ishida, M.; Zhou, H. Understanding sodium-ion diffusion in layered P2 and P3 oxides via experiments and first-principles calculations: a bridge between crystal structure and electrochemical performance. *NPG Asia Mater.* **2016**, 8 (4), e266-e266. https://doi.org/10.1038/am.2016.53.
- (24) Billaud, J.; Clément, R. J.; Armstrong, A. R.; Canales-Vázquez, J.; Rozier, P.; Grey, C. P.; Bruce, P.
 G. β-NaMnO₂: A High-Performance Cathode for Sodium-Ion Batteries. *J. Am. Chem. Soc.* 2014, *136*(49), 17243-17248. https://doi.org/10.1021/ja509704t.
- (25) Mendiboure, A.; Delmas, C.; Hagenmuller, P. Electrochemical intercalation and deintercalation of NaxMnO2 bronzes. *J. Solid State Chem.* **1985**, *57* (3), 323-331. https://doi.org/10.1016/0022-4596(85)90194-X.
- (26) Caballero, A.; Hernán, L.; Morales, J.; Sánchez, L.; Santos Peña, J.; Aranda, M. A. G. Synthesis and characterization of high-temperature hexagonal P2-Na_{0.6} MnO₂ and its electrochemical behaviour as cathode in sodium cells. *J. Mater. Chem.* **2002**, *12* (4), 1142-1147, 10.1039/B108830K. https://doi.org/10.1039/B108830K.
- (27) Yang, L.; Luo, S.-h.; Wang, Y.; Zhan, Y.; Wang, Q.; Zhang, Y.; Liu, X.; Mu, W.; Teng, F. Cu-doped layered P2-type Na_{0.67}Ni_{0.33-x}Cu_xMn_{0.67}O₂ cathode electrode material with enhanced electrochemical performance for sodium-ion batteries. *Chem. Eng. J.* **2020**, *404*, 126578. https://doi.org/10.1016/j.cej.2020.126578.

- (28) Kang, W.; Yu, D. Y. W.; Lee, P.-K.; Zhang, Z.; Bian, H.; Li, W.; Ng, T.-W.; Zhang, W.; Lee, C.-S. P2-Type Na_xCu_{0.15}Ni_{0.20}Mn_{0.65}O₂ Cathodes with High Voltage for High-Power and Long-Life Sodium-Ion Batteries. *ACS Appl. Mater. Interfaces* **2016**, *8* (46), 31661-31668. https://doi.org/10.1021/acsami.6b10841.
- (29) Kang, W.; Zhang, Z.; Lee, P.-K.; Ng, T.-W.; Li, W.; Tang, Y.; Zhang, W.; Lee, C.-S.; Wai Yu, D. Y. Copper substituted P2-type Na_{0.67}Cu_xMn_{1-x}O₂: a stable high-power sodium-ion battery cathode. *J. Mater. Chem. A* **2015**, *3* (45), 22846-22852. https://doi.org/10.1039/C5TA06371J.
- (30) Liu, H.; Gao, X.; Chen, J.; Gao, J.; Yin, S.; Zhang, S.; Yang, L.; Fang, S.; Mei, Y.; Xiao, X.; et al. Reversible OP4 phase in P2–Na_{2/3}Ni_{1/3}Mn_{2/3}O₂ sodium ion cathode. *J. Power Sources* **2021**, *508*, 230324. https://doi.org/10.1016/j.jpowsour.2021.230324.
- (31) Feng, J.; Luo, S.-h.; Dou, Y.; Cong, J.; Liu, X.; Li, P.; Yan, S.; Wang, Q.; Zhang, Y.; Lei, X.; et al. Facile design and synthesis of Co-free layered O3-type NaNi_{0.2}Mn_{0.2}Fe_{0.6}O₂ as promising cathode material for sodium-ion batteries. *J. Electroanal. Chem.* **2022**, *914*, 116301. https://doi.org/10.1016/j.jelechem.2022.116301.
- (32) Feng, J.; Luo, S.-h.; Wang, J.; Li, P.; Yan, S.; Li, J.; Hou, P.-q.; Wang, Q.; Zhang, Y.; Liu, X. Stable Electrochemical Properties of Magnesium-Doped Co-Free Layered P2-Type Na_{0.67}Ni_{0.33}Mn_{0.67}O₂ Cathode Material for Sodium Ion Batteries. *ACS Sustainable Chemistry & Engineering* **2022**, *10* (15), 4994-5004. 10.1021/acssuschemeng.2c00197.
- (33) Chen, T.; Liu, W.; Liu, F.; Luo, Y.; Zhuo, Y.; Hu, H.; Guo, J.; Yan, J.; Liu, K. Benefits of Copper and Magnesium Cosubstitution in Na_{0.5}Mn_{0.6}Ni_{0.4}O₂ as a Superior Cathode for Sodium Ion Batteries. *ACS Appl. Energy Mater.* **2019**, *2* (1), 844-851. https://doi.org/10.1021/acsaem.8b01909.
- (34) Yuan, D.; Hu, X.; Qian, J.; Pei, F.; Wu, F.; Mao, R.; Ai, X.; Yang, H.; Cao, Y. P2-type Na_{0.67}Mn_{0.65}Fe_{0.2}Ni_{0.15}O₂ Cathode Material with High-capacity for Sodium-ion Battery. *Electrochim. Acta* **2014**, *116*, 300-305. DOI: https://doi.org/10.1016/j.electacta.2013.10.211.

- (35) Talaie, E.; Kim, S. Y.; Chen, N.; Nazar, L. F. Structural Evolution and Redox Processes Involved in the Electrochemical Cycling of P2–Na_{0.67}[Mn_{0.66}Fe_{0.20}Cu_{0.14}]O₂. *Chem. Mater.* **2017**, *29* (16), 6684-6697. https://doi.org/10.1021/acs.chemmater.7b01146.
- (36) Wang, Y.; Kim, S.; Lu, J.; Feng, G.; Li, X. A Study of Cu Doping Effects in P2-Na_{0.75}Mn0.6Fe0.2(CuxNi0.2-x)O2 Layered Cathodes for Sodium-Ion Batteries. *Batter. Supercaps* **2020**, *3* (4), 376-387. https://doi.org/10.1002/batt.201900172.
- (37) Wang, L.; Sun, Y.-G.; Hu, L.-L.; Piao, J.-Y.; Guo, J.; Manthiram, A.; Ma, J.; Cao, A.-M. Coppersubstituted Na_{0.67}Ni_{0.3-x}Cu_xMn_{0.7}O₂ cathode materials for sodium-ion batteries with suppressed P2–O2 phase transition. *J. Mater. Chem. A* **2017**, *5* (18), 8752-8761, 10.1039/C7TA00880E. https://doi.org/10.1039/C7TA00880E.
- (38) Zhang, Y.; Zhang, R.; Huang, Y. Air-Stable Na_xTMO₂ Cathodes for Sodium Storage. *Front. Chem.* **2019**, 7, Review. https://doi.org/10.3389/fchem.2019.00335.
- (39) Li, Y.; Yang, Z.; Xu, S.; Mu, L.; Gu, L.; Hu, Y.-S.; Li, H.; Chen, L. Air-Stable Copper-Based P2-Na_(7/9)Cu_(2/9)Fe_(1/9)Mn_(2/3)O₍₂₎ as a New Positive Electrode Material for Sodium-Ion Batteries. *Adv. Sci.* (Weinh) **2015**, *2* (6), 1500031-1500031. DOI: https://doi.org/10.1002/advs.201500031 PubMed. (40) Gutierrez, A.; Dose, W. M.; Borkiewicz, O.; Guo, F.; Avdeev, M.; Kim, S.; Fister, T. T.; Ren, Y.;
- Bareño, J.; Johnson, C. S. On Disrupting the Na⁺-Ion/Vacancy Ordering in P2-Type Sodium–Manganese–Nickel Oxide Cathodes for Na⁺-Ion Batteries. *J. Phys. Chem. C* **2018**, *122* (41), 23251-23260. https://doi.org/10.1021/acs.jpcc.8b05537.
- (41) Wang, P.-F.; Yao, H.-R.; Liu, X.-Y.; Yin, Y.-X.; Zhang, J.-N.; Wen, Y.; Yu, X.; Gu, L.; Guo, Y.-G. Na⁺ vacancy disordering promises high-rate Na-ion batteries. *Sci. Adv.* **2018**, *4* (3), eaar6018. DOI: https://doi.org/10.1126/sciadv.aar6018.
- (42) Toumar, A. J.; Ong, S. P.; Richards, W. D.; Dacek, S.; Ceder, G. Vacancy Ordering in O3-Type Layered Metal Oxide Sodium-Ion Battery Cathodes. *Phys. Rev. Appl.* **2015**, *4* (6), 064002. https://doi.org/10.1103/PhysRevApplied.4.064002.

- (43) Ma, L. A.; Palm, R.; Nocerino, E.; Forslund, O. K.; Matsubara, N.; Cottrell, S.; Yokoyama, K.; Koda, A.; Sugiyama, J.; Sassa, Y.; et al. Na-ion mobility in P2-type Na_{0.5}Mg_xNi_{0.17-x}Mn_{0.83}O₂ (0 ≤ x ≤ 0.07) from electrochemical and muon spin relaxation studies. *Phys. Chem. Chem. Phys.* **2021**, *23* (42), 24478-24486, 10.1039/D1CP03115E. https://doi.org/10.1039/D1CP03115E.
- (44) Yoshida, H.; Yabuuchi, N.; Kubota, K.; Ikeuchi, I.; Garsuch, A.; Schulz-Dobrick, M.; Komaba, S. P2-type Na_{2/3}Ni_{1/3}Mn_{2/3-x}Ti_xO₂ as a new positive electrode for higher energy Na-ion batteries. *Chem. Commun.* **2014**, *50* (28), 3677-3680, 10.1039/C3CC49856E. https://doi.org/10.1039/C3CC49856E.
- (45) Zhang, X.-H.; Pang, W.-L.; Wan, F.; Guo, J.-Z.; Lü, H.-Y.; Li, J.-Y.; Xing, Y.-M.; Zhang, J.-P.; Wu, X.-L. P2–Na_{2/3}Ni_{1/3}Mn_{5/9}Al_{1/9}O₂ microparticles as superior cathode material for sodium-ion batteries: enhanced properties and mechanism via graphene connection. *ACS Appl. Mater. Interfaces* **2016**, *8* (32), 20650-20659. https://doi.org/10.1021/acs.chemmater.5b04557.
- (46) Wu, X.; Guo, J.; Wang, D.; Zhong, G.; McDonald, M. J.; Yang, Y. P2-type Na_{0.66}Ni_{0.33-x}Zn_xMn_{0.67}O₂ as new high-voltage cathode materials for sodium-ion batteries. *J. Power Sources* **2015**, *281*, 18-26. https://doi.org/10.1016/j.jpowsour.2014.12.083.
- (47) Marelli, E.; Villevieille, C.; Park, S.; Hérault, N.; Marino, C. Co-Free P2–Na_{0.67}Mn_{0.6}Fe_{0.25}Al_{0.15}O₂ as Promising Cathode Material for Sodium-Ion Batteries. *ACS Appl. Energy Mater.* **2018**, *I* (11), 5960-5967. https://doi.org/10.1021/acsaem.8b01015.
- (48) Wang, Q.-C.; Hu, E.; Pan, Y.; Xiao, N.; Hong, F.; Fu, Z.-W.; Wu, X.-J.; Bak, S.-M.; Yang, X.-Q.; Zhou, Y.-N. Utilizing Co²⁺/Co³⁺ Redox Couple in P2-Layered Na_{0.66}Co_{0.22}Mn_{0.44}Ti_{0.34}O₂ Cathode for Sodium-Ion Batteries. *Advanced Science* **2017**, *4* (11), 1700219. DOI: https://doi.org/10.1002/advs.201700219.
- (49) Lan, T.; Wei, W.; Xiao, S.; He, G.; Hong, J. P2-type Fe and Mn-based Na_{0.67}Ni_{0.15}Fe_{0.35}Mn_{0.3}Ti_{0.2}O₂ as cathode material with high energy density and structural stability for sodium-ion batteries. *J. Mater. Sci. Mater. Electron.* **2020**, *31* (12), 9423-9429. https://doi.org/10.1007/s10854-020-03482-9.

- (50) Cao, Z.; Li, L.; Zhou, C.; Ma, X.; Wang, H. Contribution of titanium substitution on improving the electrochemical properties of P2-Na_{0.67}Ni_{0.33}Mn_{0.67}O₂ cathode material for sodium-ion storage. *Funct. Mater. Lett.* **2020**, *13* (03), 2051010. DOI: https://doi.org/10.1142/S1793604720510108.
- (51) Li, Z.-Y.; Gao, R.; Sun, L.; Hu, Z.; Liu, X. Zr-doped P2-Na_{0.75}Mn_{0.55}Ni_{0.25}Co_{0.05}Fe_{0.10}Zr_{0.05}O₂ as high-rate performance cathode material for sodium ion batteries. *Electrochim. Acta* **2017**, *223*, 92-99. https://doi.org/10.1016/j.electacta.2016.12.019.
- (52) Milewska, A.; Zając, W.; Trenczek-Zając, A.; Molenda, J. Cobalt-free copper-substituted Na(Ti,Mn,Ni,Cu)O2 layered oxide cathode materials for Na-ion batteries. *J. Solid State Chem.* **2022**, *315*, 123461. https://doi.org/10.1016/j.jssc.2022.123461.
- (53) Tan, L.; Wu, Q.; Liu, Z.; Chen, Q.; Yi, H.; Zhao, Z.; Song, L.; Zhong, S.; Wu, X.; Li, L. Tisubstituted O3-type layered oxide cathode material with high-voltage stability for sodium-ion batteries. *J. Colloid Interface Sci.* **2022**, *622*, 1037-1044. https://doi.org/10.1016/j.jcis.2022.04.112.
- (54) Feng, J.; Luo, S.-h.; Sun, M.; Cong, J.; Yan, S.; Wang, Q.; Zhang, Y.; Liu, X.; Mu, W.; Hou, P.-q. Investigation of Ti-substitution and MnPO₄ coating effects on structural and electrochemical properties of P2-Na_{0.67}Ti_xNi_{0.33}Mn_{0.67-x}O₂ cathode materials. *Appl. Surf. Sci.* **2022**, *600*, 154147. https://doi.org/10.1016/j.apsusc.2022.154147.
- (55) Vasavan, H. N.; Badole, M.; Dwivedi, S.; Kumar, S. Structural and transport properties of P2-Type Na_{0.70}Ni_{0.20}Cu_{0.15}Mn_{0.65}O₂ layered oxide. *Ceram. Int.* **2022**, *48* (19, Part B), 28986-28993. https://doi.org/10.1016/j.ceramint.2022.04.206.
- (56) Vasavan, H. N.; Badole, M.; Dwivedi, S.; Kumar, D.; Kumar, P.; Kumar, S. Enhanced rate performance and specific capacity in Ti-substituted P2-type layered oxide enabled by crystal structure and particle morphology modifications. *Chem. Eng. J.* **2022**, *448*, 137662. https://doi.org/10.1016/j.cej.2022.137662.

- (57) Coelho, A. TOPAS and TOPAS-Academic: an optimization program integrating computer algebra and crystallographic objects written in C++. *J. Appl. Crystallogr.* **2018**, *51* (1), 210-218. https://doi.org/10.1107/S1600576718000183.
- (58) Tang, K.; Huang, Y.; Xie, X.; Cao, S.; Liu, L.; Liu, H.; Luo, Z.; Wang, Y.; Chang, B.; Shu, H.; et al. Electrochemical performance and structural stability of air-stable Na_{0.67}Ni_{0.33}Mn_{0.67-x}Ti_xO₂ cathode materials for high-performance sodium-ion batteries. *Chem. Eng. J.* **2020**, *399*, 125725. https://doi.org/10.1016/j.cej.2020.125725.
- (59) Park, J.-k.; Park, G.-g.; Kwak, H. H.; Hong, S.-T.; Lee, J.-w. Enhanced Rate Capability and Cycle Performance of Titanium-Substituted P2-Type Na_{0.67}Fe_{0.5}Mn_{0.5}O₂ as a Cathode for Sodium-Ion Batteries. *ACS Omega* **2018**, *3* (1), 361-368. DOI: https://doi.org/10.1021/acsomega.7b01481.
- (60) Shannon, R. Revised effective ionic radii and systematic studies of interatomic distances in halides and chalcogenides. *Acta Crystallogr. A* **1976**, *32* (5), 751-767. https://doi.org/10.1107/S0567739476001551.
- (61) Momma, K.; Izumi, F. VESTA 3 for three-dimensional visualization of crystal, volumetric and morphology data. *J. Appl. Crystallogr.* **2011**, *44* (6), 1272-1276. https://doi.org/10.1107/S0021889811038970.
- (62) Moulder, J. F.; Chastain, J. Handbook of X-ray Photoelectron Spectroscopy: A Reference Book of Standard Spectra for Identification and Interpretation of XPS Data; Physical Electronics Division, Perkin-Elmer Corporation, 1992.
- (63) Hüfner, S. *Photoelectron spectroscopy: principles and applications*; Springer Science & Business Media, 2013.
- (64) Li, Z.-Y.; Gao, R.; Sun, L.; Hu, Z.; Liu, X. Designing an advanced P2-Na_{0.67}Mn_{0.65}Ni_{0.2}Co_{0.15}O₂ layered cathode material for Na-ion batteries. *J. Mater. Chem. A* **2015**, *3* (31), 16272-16278, https://doi.org/10.1039/C5TA02450A.

- (65) Bucher, N.; Hartung, S.; Franklin, J. B.; Wise, A. M.; Lim, L. Y.; Chen, H.-Y.; Weker, J. N.; Toney, M. F.; Srinivasan, M. P2–Na_xCo_yMn_{1-y}O₂ (y = 0, 0.1) as Cathode Materials in Sodium-Ion Batteries—
 Effects of Doping and Morphology To Enhance Cycling Stability. *Chem. Mater.* 2016, 28 (7), 2041-2051.
 https://doi.org/10.1021/acs.chemmater.5b04557.
- (66) Li, Z.-Y.; Zhang, J.; Gao, R.; Zhang, H.; Zheng, L.; Hu, Z.; Liu, X. Li-Substituted Co-Free Layered P2/O3 Biphasic Na_{0.67}Mn_{0.55}Ni_{0.25}Ti_{0.2-x}Li_xO₂ as High-Rate-Capability Cathode Materials for Sodium Ion Batteries. *J. Phys. Chem. C* **2016**, *120* (17), 9007-9016. https://doi.org/10.1021/acs.jpcc.5b11983.
- (67) Pei, Q.; Lu, M.; Liu, Z.; Li, D.; Rao, X.; Liu, X.; Zhong, S. Improving the Na_{0.67}Ni_{0.33}Mn_{0.67}O₂
 Cathode Material for High-Voltage Cyclability via Ti/Cu Codoping for Sodium-Ion Batteries. *ACS Appl. Energy Mater.* **2022**, *5* (2), 1953-1962. https://doi.org/10.1021/acsaem.1c03466.
- (68) Wu, X.; Xu, G.-L.; Zhong, G.; Gong, Z.; McDonald, M. J.; Zheng, S.; Fu, R.; Chen, Z.; Amine, K.; Yang, Y. Insights into the Effects of Zinc Doping on Structural Phase Transition of P2-Type Sodium Nickel Manganese Oxide Cathodes for High-Energy Sodium Ion Batteries. *ACS Appl. Mater. Interfaces* **2016**, *8* (34), 22227-22237. https://doi.org/10.1021/acsami.6b06701.